

# A unified Benchmark for Multi-Frame Image Restoration under Severe Refractive Warping

Maxim V. Shugaev<sup>1</sup>, Md Reshad Ul Hoque<sup>1</sup>, Bridget Kennedy<sup>1</sup>, Joseph T. Riley<sup>1</sup>, Fiona Hwang<sup>1</sup>, Justin Hagen<sup>2,3</sup>, Harvir Ghuman<sup>2</sup>, Ethan Garcia-O'Donnell<sup>2</sup>, Syed Noor Qadri<sup>2</sup>, Freddie Santiago<sup>2</sup>, Mun Wai Lee<sup>1</sup>

<sup>1</sup>AeroVironment, Inc.

<sup>2</sup>U. S. Naval Research Laboratory

<sup>3</sup>George Mason University

maxim.shugaev@avinc.com

## Abstract

*Video sequence capturing through refractive dynamic media, such as a turbulent air or water surface, often suffer from severe geometric distortions and temporal instability. While recent advances address mild atmospheric turbulence, no existing benchmarks systematically evaluate restoration methods under strong and highly nonuniform refractive conditions. We present a comprehensive benchmark for geometric distortion removal in video, covering a range from turbulence-like mild warping to strong discontinuous refractive deformations. The benchmark includes both laboratory-captured real data and synthetic sequences generated for static scenes via physics-based light refraction modeling across four distortion levels and multiple surface wave types. We evaluate a spectrum of methods from simple baselines and classical registration algorithms to advanced learning-based approaches including DATUM and our proposed diffusion based V-cache for high and extreme distortions regimes. Evaluation uses both pixel-level (PSNR, SSIM), and perceptual (LPIPS, DINO, CLIP) metrics providing the first large scale analysis of geometric distortion removal. Our benchmark establishes a new foundation for developing and evaluating algorithms capable of reconstructing video from highly distorted optical environments. Our code and datasets are available at <https://github.com/iafoss/refractive-mfir-benchmark>.*

**Keywords:** Video restoration, Geometric warping, Water-surface refraction, Benchmark dataset, Diffusion models

## 1. Introduction and Related Work

Recovering visually coherent video from imagery degraded by extreme geometric distortions remains a fundamental and unsolved problem in computational imaging. Unlike

additive noise, blur, or compression artifacts, these distortions arise from nonlinear refraction phenomena, e.g., atmospheric turbulence, dynamic water surface and Snell's law, or nonuniform thermal gradients in the transparent hot air, which warp the optical waveform before it reaches the sensor. The result is a sequence of frames that are spatially misaligned and temporary inconsistent, with additional blur introduced by the rapid, time-varying refractive flow during each exposure. Despite a progress in recent years in mitigating turbulence or moderate distortions, there is still no general benchmark capturing a full range of severe spatiotemporal chaotic geometric degradations observed in real environment.

Prior work has addressed the specific subdomains of the problem. Atmospheric turbulence mitigation datasets focus on long-range imaging through air, e.g., CLEAR [1, 2], DOST [3], and UG2+ [4], and provide synthetic and real sequences degraded by mild to moderate distortion. These datasets enable evaluation of alignment methods, e.g. lucky imaging [5], DATUM [6], PiRN [7], but largely assume small displacements and smooth temporal evolution. At the other side, work on through-water imaging has explored the effects of dynamic water-air interface (WAI), where wave-induced refraction introduces stronger rapidly varying geometric distortion. Unfortunately, publicly available datasets [8–10] are relatively small and focus on the medium level of distortion. The Sea-Undistort [11] dataset primarily considers color attenuation and scattering rather than the deformation field. In addition, while synthetic data provide paired distorted and undistorted imagery for supervised learning and evaluation, there is a lack of real world videos and there remains a domain gap where the synthetic data fails to capture realistic turbulent wave surfaces, lighting variations, and complex scenes. Outside of these domains, video restoration datasets are primarily focused on video deblurring and optical flow estimation. Consequently, current datasets cannot comprehensively measure the model's

ability to handle large, spatially incoherent, and rapid distortions, leaving a major gap between synthetic turbulence evaluation and the challenges observed in real refractive environments.

Previous work for mitigating geometric distortions in video may be grouped into three broad categories: physics-based analytical modeling, multi-frame fusion methods, and learning-based approaches. Analytical approaches attempt to explicitly model the WAI geometry and refraction effect. Jian et al. [12] used structured-light projection to estimate the instantaneous water surface geometry and applied reverse ray tracing for single image restoration, which was later refined using Helmholtz-Hodge decomposition of the distortion field [13]. Qian et al. [14] used a camera array to jointly perform 3D reconstruction of the water surface and reconstruct the scene. These analytical approaches require complex hardware setup and calibration.

Multi-frame fusion approaches do not require special hardware but instead use multiple frames to estimate a stable image of a static scene. Zhang et al. [15] used a patch-based iterative registration approach combined with blind deconvolution algorithm to construct a reference frame. Jian et al. [16] used global optimization JADE algorithm and a local optimization LBFGS algorithm to perform non-rigid image registration efficiently. Li *et al.* [17] use an approach inspired by NERF on training a model predicting deformation grids and the undistorted image for a given image sequence. These methods struggle with low texture scenes and strong image distortions.

In the third category, learning-based image restoration methods learn to estimate and reverse image distortions using data driven or deep neural network models. DATUM [6] blends ideas from classical multi-frame methods as frame alignment, lucky patch fusion, blind deconvolution into a recurrent network architecture that performs temporal aggregation. MambaTM [18] expands this approach with selective state space model to expand the receptive field. Thapa *et al.* [19] trained a distortion-guided network (DG-NET) to predict the distortion-free underwater image. Li *et al.* [20] used a generative adversarial network (GAN) with an attention-based encoder-decoder architecture to remove spatially varying refractive distortions. Such learning-based methods require large training data, which are often simulated, and therefore are limited by the domain gap between synthetic and real-world distortions. Furthermore, since existing benchmarks mostly capture mild to medium levels of distortion, these models are not systematically evaluated in extreme regimes.

We introduce a comprehensive benchmark for removal of extreme geometric distortion from a sequence of frames, designed to bridge the gap between atmospheric turbulence mitigation and WAI refractive scenarios. The benchmark focuses on light propagating through dynamic water sur-

faces, modeling surface perturbations that produce a range of image degradations from mild distortions, comparable to turbulence mitigation, to extreme regimes. These regimes are characterized by discontinuities and multiple apparent instances of the same objects caused by strongly nonlinear image mapping due to multi-path refraction from a dynamic surface. In addition, we propose V-cache, a novel multi-frame diffusion method for effective restoring videos degraded by high and extreme levels of geometric distortions. In summary, our contributions are the following:

1. A comprehensive benchmark dataset for extreme geometric distortion removal from video, including both laboratory-captured real sequences and synthetic data generated for static scenes under controlled conditions.
2. A systematically synthetic dataset design that varies distortion amplitude and surface wave type (with surface normal derived from physically based water wave simulation), producing a continuum of refractive conditions from turbulence-like mild warping to severe discontinuous deformations.
3. Evaluation covering a wide range of approaches from simple baselines (first-frame and mean-frame fusion), through multi-frame registration (e.g. grid deformation [17]), to modern learning based models such as DATUM [6] and our proposed V-cache.
4. A unified evaluation protocol combining pixel-based (PSNR, SSIM) and perception (LPIPS, DINO, CLIP) metrics, allowing rigorous and perceptually consistent assessment.

## 2. Dataset

### 2.1. Synthetic data

The synthetic data is constructed by combining a particular image background with a wave profile. We consider four distinct types of waves: ocean, shallow water, sine, and ripples with details provided below and in the Supplement. In total, the synthetic evaluation set contains of 30 backgrounds and 10 200-frame-long wave profiles for each wave, and we select a fixed subset of 60 combinations as the final benchmark. We adjust the wave amplitude in the generation process and consider 4 amplitude levels: low, mid, high, and extreme, which correspond to 0.002, 0.006, 0.018, and 0.054 average *std* displacement (relative to the image size) over 10 considered profiles for a given wave type. The speed of waves is selected to maintain a comparable rate of distortion for all wave types. Examples illustrating the corresponding degree of image distortion are shown in Figure 1. The above combinations produce 16 benchmarks accounting for different wave types and decrease of distortion. The wave profiles, background images, and the code generating the evaluation data are available at ref. [21, 22]



Figure 1. An illustration of the distortion level for different wave amplitudes for ocean waves. Since low and mid amplitudes provide minimal perceptual distortion, we also present the mean pixel values averaged over the entire image sequence.

## 2.2. Real data

The LAB data collection contains a set of undistorted views paired with video recorded in presence of waves. In this set up, a large water tank ( $20 \times 7 \times 3$  feet) was filled with approximately 19-inch depth of water. A TV monitor was placed above the water to display a set of background images. The camera was set up below the water tank pointing towards the TV. During video recording, a programmable wave generator at one end of the water tank produced disturbance on the water surface with a sine wave profile of a frequency between 1.0 to 2.8 Hz and wave amplitude ranging from 3 to 15 mm peak-to-peak. Besides the sine wave generator, two water pumps were used to generate additional random ripple-like waves. A schematic layout of the data collection hardware is provided in the supplementary material.

We divide the collected videos into 200 frame clips and resize to  $512 \times 512$  pixels to have a uniform framework for evaluation. The total number of clips is 216 that combines cases both with low and high levels of distortions.

## 3. Baseline Experiments

### 3.1. Baseline Models

In our analysis we consider the following approaches. *First frame* – select the first frame of the input video as a prediction, which serves as a reference characterizing the degree of distortion. *Pixel average* – temporally average values of pixels and present it as a prediction.

The next set of models is based on recovery of deformation grids corresponding to the distortion in the input. *Grid deformation* (Non-Rigid Image Distortion Removal) is a self-supervised method described in ref. [17]. Specifically, given a sequence of distorted frames, the method employs a trainable grid prediction network to estimate the non-rigid deformation field, and a frame reconstruction network that is conditioned on this field to generate the restored image.

During training the model learns two complementary mappings: when conditioned on deformed grids, the reconstruction network is supervised to reproduce the corresponding distorted frame, while for a uniform grid, it is expected to produce undistorted (restored) image. The restored output is then warped with predicted deformation field and matched to the input frames. This approach involves training the models for each input sequence and therefore is extremely computational expensive. To keep the inference manageable we downscale input sequence to  $256 \times 256$  and select only first 11 frames with stride of 2, which reduces the time to approximately 5.2 minutes per sequence.

Another approach is *Grid registration*, which may be considered as a simplified version of *Grid deformation* where the trainable deformation grids are defined explicitly and applied through warp operation. We assign a coarse learnable grid deformation (1 grid point per  $16 \times 16$  pixels) to each frame and maximize all vs. all pixel similarity between frames in the video as the optimization objective. Basically this method fits transformations that bring a sequence of distorted frames towards the same appearance, which approximate the static scene. For long sequence, to avoid square increase of the computational complexity, we limit the number of comparisons for each frame by 12 random frames. We apply regularization to prevent large grid deformation or drift. The grid optimization is performed at  $256 \times 256$  input size, but we warp the original input rather than reduced one with the grid to mitigates blur (which is apparent in *Grid deformation* output) and improve perception metrics. In addition, better computational efficiency enables running this method on the entire 200-frame-long input resulting in the runtime of 39 seconds per sequence.

*DATUM* [6] is a deep-learning based approach designed to remove distortions in a sequence of images caused by atmospheric turbulence. This approach blends ideas from classical multi-frame methods as frame alignment, lucky patch fusion, blind deconvolution into a recurrent network

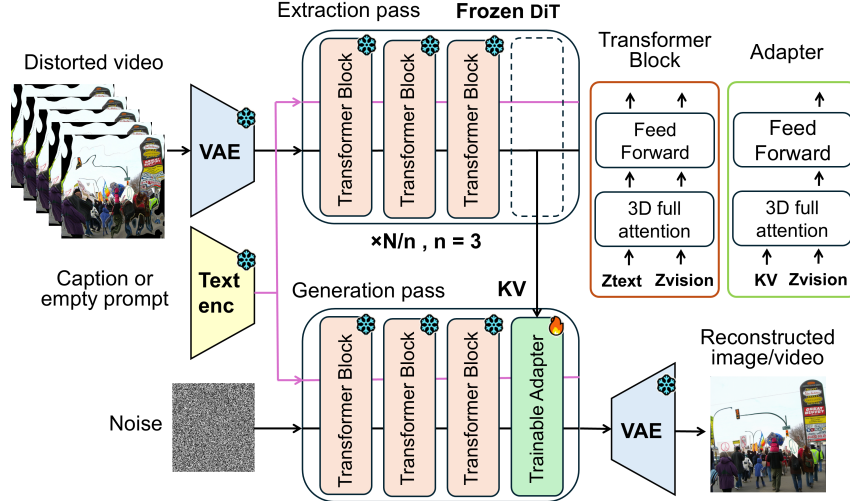


Figure 2. Schematic illustration of V-cache.  $N$  refers to the total number of transformer blocks in the model.

architecture that performs temporal aggregation. Within the network modules like deformable attention alignment and temporal channel attention handle pixel registration and selective fusion, while the twin decoder jointly corrects tilt and blur degradations. In the turbulence problem DATUM archives superior performance and runs several orders of magnitude faster than prior methods taking sub-second time per sequence. Despite this success, the model design limitations, *i.e.* limited receptive field, local feature aggregation, coarse hierarchical flow estimation, and short temporal content aggregation may provide a challenge for modeling rapidly changing strong distortions. Specifically, in our experiments, fine-tuning the model on mid-to-high-amplitude ocean waves caused the appearance of artifacts and degraded performance. Therefore, in our comparison, we use only the original model weights. The inference is performed at  $512 \times 512$  resolution with 49-frame-long sequences.

*V-cache.* Recent advancements of diffusion models, which gradually transform random noise into output through a sequence of denoising steps, have enabled high quality text-to-image and text-to-video generation [23–27]. Public availability of diffusion models [24, 27–29] has facilitated efforts to enable controllable generation beyond conditioning on text [30–33]. The current task of heavy distortion removal may be considered as image or video generation (in case of dynamic scenes) conditioned on another video. Since the output is not pixel aligned with the input, ControlNet-like methods [30] are ineffective. Therefore, as a starting point we considered an encoder-based method: extraction of features from a sequence of frames with DINO [34] encoder and finetuning the diffusion model conditioned on these features. Despite the ability of this method to remove the distortion, proper feature alignment is problematic, and reproduction of fine details of the input

video, *e.g.* text, is difficult. One of the recent works [35] considers a problem of personalized image generation using a reference-based method conditioning generation directly based on features extracted by the diffusion denoiser. We follow the same logic in the method proposed in our work, Figure 2. Specifically, first we extract features from the distorted video input at zeroth denoising step and cache them. Then the denoising process is conditioned by these cached features with using adapters inserted into the denoiser (Figure 2).

As the base model we chose CogVideoX-2B [28] because it performs temporal compression in VAE and has full cross-attention between all frames enabling effective input interpretation even under conditions of strong and fast distortions. During training, the base model is frozen, and injection of features is performed with learnable adapters containing cross-attention followed with MLP, as illustrated in Figure 2. The adapters are inserted after every 5th and 3rd layers, A5 and A3 setups, respectively, which correspond to 180M and 300M trainable parameters in total.

At the generation stage we consider single frame output since the scene is static, but the method is expandable to dynamic scenes with generating a sequence of frames. The total number of processed samples in training is approximately 2.5M, and we dynamically generate samples randomly mixing precomputed wave profiles and backgrounds, as described in the section on synthetic data generation. The model is trained only on ocean wave samples at high wave amplitude range to explore capabilities of this method in removing strong distortions unreachable by registration and DATUM like methods. In contrast to previously published use cases of adapters for reference-based methods [35, 36], where the model extracts an object from one content and places it to another one, in this setup the model is required

to reconstruct the undeformed view across multiple frames with high degree of distortion. Therefore, training is relatively long taking 50k steps with 48 batch size. For the 49-frame input setup, the training takes about one month on six A6000 GPUs. We use the native model resolution of 480×720, and at evaluation the input/output is resized from and to 512×512, which may lead to underestimation of the model performance especially in low distortion regime. The inference time is approximately 10 seconds per sequence.

### 3.2. Metrics

We use pixel based and perception metrics to evaluate the quality of image restoration in the considered distortion removal task. PSNR (Peak Signal-to-Noise Ratio) and SSIM (Structural Similarity Index) [37] are classical reference-based metrics that measure pixel level fidelity. PSNR emphasizes exact intensity matching, rewarding images that resemble the ground truth, while SSIM models track local luminance, contrast, and structural similarity more precisely. These metrics are simple and interpretable but struggle with correct assessment of blurry or slightly misaligned input, failing to reflect human visual quality perception.

Perception metrics, e.g. LPIPS (Learned Perceptual Image Patch Similarity) [38], DINO and CLIP scores [39], use deep feature embeddings from pretrained networks to assess high level visual similarity. LPIPS measures the differences in intermediate CNN features, which is aligned with human perception of sharpness and texture. DINO and CLIP scores provide one more step forward utilizing high quality foundational models as a feature extractor, providing the best agreement with human perception of quality. Use of transformer-based global representations enables capturing scene level coherence as well. However, these metrics can overlook fine structural errors and may over reward perceptually plausible but geometrically inaccurate outputs. In our work, LPIPS is evaluated using features from the VGG network if not specified explicitly, and we use  $L_2$  distance between intermediate features for *dinov1* and *clip\_vitb32* models, which are referred to as DINO and CLIP, respectively.

### 3.3. Results and discussion

Tables 1-3 summarize the performance of the considered methods on the benchmarks we established. We report results only on low and high wave amplitudes and PSNR, LPIPS, and DINO metrics due to the size limitation, while the full set of results is provided in the Supplement. At the low wave amplitude, comparable to the distortion level introduced by air turbulence, the best results are demonstrated by DATUM and grid registration. Despite DATUM is trained on atmospheric turbulence, it exhibits competitive performance on our benchmark in low distortion case, and further finetuning of the model could boost the performance in this regime. Lower relative performance of V-cache in



Figure 3. Example of the output produced by V-cache A5 and A3 configurations on the input with extreme distortion level.

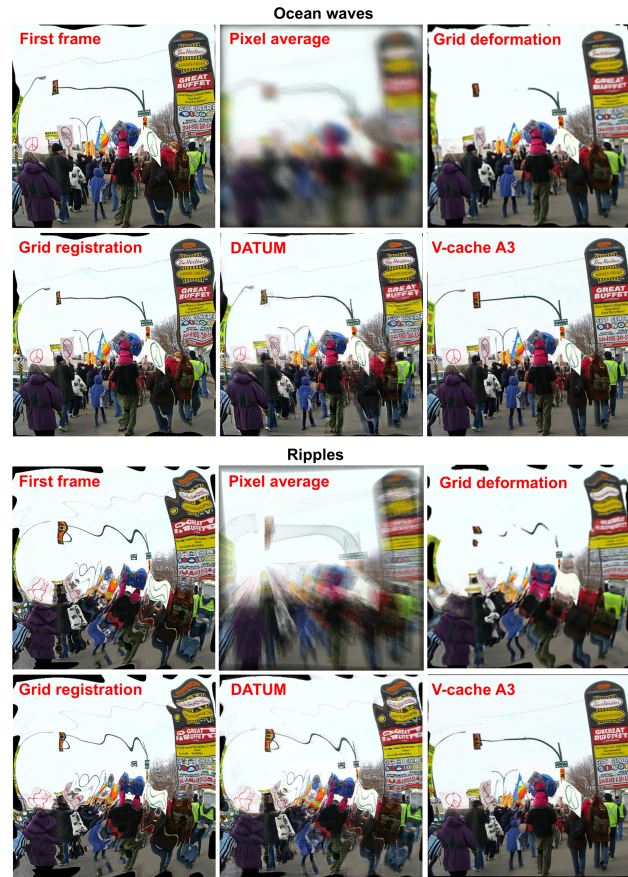


Figure 4. Example of the output for ocean waves and ripples at high wave amplitude.

low distortion regime may be explained by the resizing of the input video and the output image and the training on

Table 1. Comparison of PSNR $\uparrow$  for synthetic waves. L, H – low and high wave amplitude. (\*) refers to evaluation on multiple output frames and average the metric.

Setup	Ocean		Shallow water		Sine		Ripples	
	L	H	L	H	L	H	L	H
First frame	23.43	14.47	21.71	13.27	21.37	13.41	20.66	13.07
Pixel average	<b>27.69</b>	17.40	<b>25.67</b>	16.52	25.82	16.78	25.01	16.41
Grid deformation	25.19	15.87	20.76	14.21	20.76	14.14	21.59	14.37
Grid registration*	25.44	15.08	24.81	13.94	25.84	14.96	<b>25.93</b>	13.12
DATUM*	26.19	15.60	23.43	13.66	<b>26.02</b>	14.94	22.07	13.88
V-cache A5	23.95	21.16	23.35	17.45	22.95	20.54	23.69	17.73
V-cache A3	24.86	<b>22.22</b>	23.92	<b>17.17</b>	23.87	<b>22.07</b>	24.02	<b>18.32</b>

Table 2. Comparison of LPIPS $\downarrow$  for synthetic waves. L, H – low and high wave amplitude. (\*) refers to evaluation on multiple output frames and average the metric.

Setup	Ocean		Shallow water		Sine		Ripples	
	L	H	L	H	L	H	L	H
First frame	0.075	0.356	0.099	0.503	0.099	0.380	0.129	0.521
Pixel average	0.172	0.608	0.204	0.612	0.196	0.521	0.214	0.556
Grid deformation	0.215	0.481	0.328	0.551	0.326	0.491	0.337	0.564
Grid registration*	<b>0.071</b>	0.366	<b>0.076</b>	0.464	<b>0.067</b>	0.327	<b>0.063</b>	0.517
DATUM*	0.125	0.457	0.137	0.533	0.121	0.454	0.172	0.553
V-cache A5	0.134	0.186	0.135	0.256	0.152	0.190	0.142	0.323
V-cache A3	0.126	<b>0.157</b>	0.125	<b>0.247</b>	0.153	<b>0.150</b>	0.142	<b>0.274</b>

Table 3. Comparison of DINO $\downarrow$  for synthetic waves. L, H – low and high wave amplitude. (\*) refers to evaluation on multiple output frames and average the metric.

Setup	Ocean		Shallow water		Sine		Ripples	
	L	H	L	H	L	H	L	H
First frame	0.34	1.98	0.49	3.16	0.41	2.22	0.68	3.43
Pixel average	0.73	3.47	0.82	3.61	0.98	3.28	1.20	3.66
Grid deformation	0.74	2.49	1.37	3.40	1.35	2.75	1.49	3.71
Grid registration*	<b>0.30</b>	2.07	<b>0.32</b>	2.79	<b>0.28</b>	1.83	<b>0.26</b>	3.34
DATUM*	0.40	2.53	0.42	3.31	0.38	2.52	0.59	3.59
V-cache A5	0.41	0.64	0.39	1.03	0.50	0.68	0.46	1.62
V-cache A3	0.37	<b>0.45</b>	0.36	<b>0.97</b>	0.55	<b>0.45</b>	0.49	<b>1.23</b>

high wave amplitude only. In addition, exact reproduction of finite image features by this method still may be challenging, which is apparent in low distortion regime. Regarding PSNR, the pixel average benchmark has quite high value, sometimes even outperforming other methods in this regime, while the resulting images are blurry and often visually look worse than the first frame benchmark Figure 1, which illustrates poor alignment of this metric with human perception.

With increase of the wave amplitude the performance of V-cache decreases only moderately compared to other

methods, and even in the case of extreme wave amplitude the model still can accurately reproduce the content of the image except ripples, Figure 3. Both perception and pixel metrics are dominated by V-cache for a range of wave amplitudes between mid and extreme. Surprisingly, despite the model was not trained on extreme wave amplitude and on waves other than ocean waves, it shows high performance on these out of domain cases and likely could be improved further by training on the specific conditions, especially the case of ripples that currently exhibit difficulties. Figure 4 shows a comparison of the output for ocean

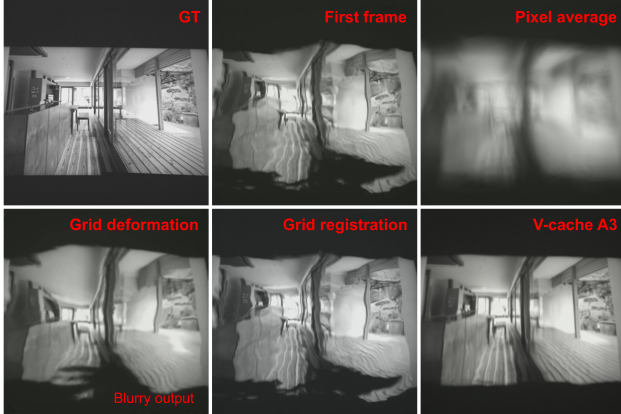


Figure 5. Example of the output for LAB data with high distortion.

Table 4. Comparison of the performance on the LAB dataset. (\*) indicates evaluation on a video and averaging the metrics.

Method	PSNR $\uparrow$	SSIM $\uparrow$	LPIPS $\downarrow$	DINO $\downarrow$
First frame	20.6	0.740	0.330	1.80
Pixel average	23.3	0.792	0.379	2.25
Grid deformation	21.0	0.752	0.387	1.89
Grid registration*	22.8	0.787	0.282	<b>0.81</b>
V-cache A5	21.1	0.755	0.349	1.80
V-cache A3	<b>23.4</b>	<b>0.831</b>	<b>0.250</b>	1.16

waves and ripples at high wave amplitude. At this level of distortion, the first frame benchmark has visible deformation, average pixel output looks blurry, and registration-based methods fail. The plot also showcases grid deformation method having blurry output, which is the reason of low values of perception metrics for this method compared to grid registration, despite using similar registration-based concept. Meanwhile, the output of V-cache remains close to the ground truth, and fine details are preserved.

Table 4 and Figure. 5 report results on the LAB evaluation benchmark, which showcase the performance on real data. Since LAB data consists of a combination of cases with various degree of distortion, the difference between reported methods is rather small with V-cache demonstrating the best performance overall. As shown in the plot, this model effectively handles large distortion on real images providing high quality reconstruction.

## 4. Conclusion

We introduce a unified benchmark for evaluating multi-frame image restoration under extreme refractive deformation, bridging a gap between atmospheric turbulence mitigation and water-surface refraction scenarios. Our benchmark provides both real and synthetic data, spanning a wide range of distortion severities and wave dynamics, enabling

systematic evaluation across multiple physical regimes. In a series of experiments, we benchmarked registration based multi-frame fusion and learning-based approaches, highlighting the strengths and limitations of current methods when faced with highly nonlinear discontinuous refractive warping. The performance of existing methods degrades rapidly as warping intensifies. In contrast, the proposed V-cache is capable of accurate recovery of the input content even under extreme distortion levels, which highlights the ability of learning-based methods to handle this regime. We release our dataset to establish a foundation for future research on video restoration under extreme geometric deformation [21, 22].

## 5. Acknowledgments

This material is based upon work supported by the Naval Research Laboratory (NRL) under Contract No. N00173-24-C-0001. Any opinions, findings and conclusions or recommendations expressed in this material are those of the authors and do not necessarily reflect the views of the Naval Research Laboratory.

## References

- [1] Nantheera Anantrasirichai, Alin Achim, Nick G Kingsbury, and David R Bull. Atmospheric turbulence mitigation using complex wavelet-based fusion. *IEEE Transactions on Image Processing*, 22(6):2398–2408, 2013. 1
- [2] Nantheera Anantrasirichai, Alin Achim, and David Bull. Atmospheric turbulence mitigation for sequences with moving objects using recursive image fusion. In *2018 25th IEEE international conference on image processing (ICIP)*, pages 2895–2899. IEEE, 2018. 1
- [3] Dehao Qin, Ripon Kumar Saha, Woojeh Chung, Suren Jayasuriya, Jinwei Ye, and Nianyi Li. Unsupervised moving object segmentation with atmospheric turbulence. In *European Conference on Computer Vision*, pages 18–37. Springer, 2024. 1
- [4] Ye Yuan, Wenhan Yang, Wenqi Ren, Jiaying Liu, Walter J Scheirer, and Zhangyang Wang. Ug<sup>2+</sup> track 2: A collective benchmark ... advancing image understanding in poor visibility environments. *arXiv preprint arXiv:1904.04474*, 2019. 1
- [5] Nicholas M Law, Craig D Mackay, and John E Baldwin. Lucky imaging: high angular resolution imaging in the visible from the ground. *Astronomy & Astrophysics*, 446(2):739–745, 2006. 1
- [6] Xingguang Zhang, Nicholas Chimitt, Yiheng Chi, Zhiyuan Mao, and Stanley H Chan. Spatio-temporal turbulence mitigation: A translational perspective. In *Proceedings of the IEEE/CVF conference on computer vision and pattern recognition*, pages 2889–2899, 2024. 1, 2, 3
- [7] Ajay Jaiswal, Xingguang Zhang, Stanley H Chan, and Zhangyang Wang. Physics-driven turbulence image restoration with stochastic refinement. In *Proceedings of the*

- IEEE/CVF international conference on computer vision*, pages 12170–12181, 2023. 1
- [8] Simron Thapa, Nianyi Li, and Jinwei Ye. Dynamic fluid surface reconstruction using deep neural network. In *Proceedings of the IEEE/CVF Conference on Computer Vision and Pattern Recognition*, pages 21–30, 2020. 1
- [9] Jerin Geo James, Pranay Agrawal, and Ajit Rajwade. Restoration of non-rigidly distorted underwater images using a combination of compressive sensing and local polynomial image representations. In *Proceedings of the IEEE/CVF International Conference on Computer Vision*, pages 7839–7848, 2019.
- [10] Yuandong Tian and Srinivasa G Narasimhan. Seeing through water: Image restoration using model-based tracking. In *2009 IEEE 12th International conference on computer vision*, pages 2303–2310. Ieee, 2009. 1
- [11] Maximilian Kromer, Panagiotis Agraftotis, and Begüm Demir. Sea-undistort: A dataset for through-water image restoration in high resolution airborne bathymetric mapping. *IEEE Geoscience and Remote Sensing Letters*, 2025. 1
- [12] Bijian Jian, Chunbo Ma, Dejian Zhu, Yixiao Sun, and Jun Ao. Seeing through wavy water–air interface: A restoration model for instantaneous images distorted by surface waves. *Future Internet*, 14(8):236, 2022. 2
- [13] Bijian Jian, Chunbo Ma, Yixiao Sun, Dejian Zhu, Xu Tian, and Jun Ao. Reconstruction of the instantaneous images distorted by surface waves via helmholtz–hodge decomposition. *Journal of Marine Science and Engineering*, 11(1):164, 2023. 2
- [14] Yiming Qian, Yinqiang Zheng, Minglun Gong, and Yee-Hong Yang. Simultaneous 3d reconstruction for water surface and underwater scene. In *Proceedings of the European Conference on Computer Vision (ECCV)*, pages 754–770, 2018. 2
- [15] Zhen Zhang and Xu Yang. Reconstruction of distorted underwater images using robust registration. *Optics express*, 27(7):9996–10008, 2019. 2
- [16] Bijian Jian, Chunbo Ma, Dejian Zhu, Qihong Huang, and Jun Ao. Water-air interface imaging: recovering the images distorted by surface waves via an efficient registration algorithm. *Entropy*, 24(12):1765, 2022. 2
- [17] Nianyi Li, Simron Thapa, Cameron Whyte, Albert W Reed, Suren Jayasuriya, and Jinwei Ye. Unsupervised non-rigid image distortion removal via grid deformation. In *Proceedings of the IEEE/CVF International Conference on Computer Vision*, pages 2522–2532, 2021. 2, 3
- [18] Xingguang Zhang, Nicholas Chimitt, Xijun Wang, Yu Yuan, and Stanley H. Chan. Learning phase distortion with selective state space models for video turbulence mitigation, 2025. 2
- [19] Simron Thapa, Nianyi Li, and Jinwei Ye. Learning to remove refractive distortions from underwater images. In *Proceedings of the IEEE/CVF International Conference on Computer Vision*, pages 5007–5016, 2021. 2, 11
- [20] Tengyue Li, Jiayi Song, Zhiyu Song, Arapat Ablimit, and Long Chen. Removing nonrigid refractive distortions for underwater images using an attention-based deep neural network. *Intelligent Marine Technology and Systems*, 2(1):25, 2024. 2
- [21] A unified benchmark for multi-frame image restoration under severe refractive warping: code and evaluation framework. <https://github.com/iafoss/refractive-mfir-benchmark>, 2026. GitHub repository. 2, 7
- [22] Refractive mfir benchmark dataset. <https://zenodo.org/records/19390086>, 2026. 2, 7
- [23] Jonathan Ho, Ajay Jain, and Pieter Abbeel. Denoising diffusion probabilistic models. *Advances in neural information processing systems*, 33:6840–6851, 2020. 4
- [24] Aditya Ramesh, Prafulla Dhariwal, Alex Nichol, Casey Chu, and Mark Chen. Hierarchical text-conditional image generation with clip latents. *arXiv preprint arXiv:2204.06125*, 1(2):3, 2022. 4
- [25] Robin Rombach, Andreas Blattmann, Dominik Lorenz, Patrick Esser, and Björn Ommer. High-resolution image synthesis with latent diffusion models. In *Proceedings of the IEEE/CVF conference on computer vision and pattern recognition*, pages 10684–10695, 2022.
- [26] Andreas Blattmann, Tim Dockhorn, Sumith Kulal, Daniel Mendelevitch, Maciej Kilian, Dominik Lorenz, Yam Levi, Zion English, Vikram Voleti, Adam Letts, et al. Stable video diffusion: Scaling latent video diffusion models to large datasets. *arXiv preprint arXiv:2311.15127*, 2023.
- [27] Yixin Liu, Kai Zhang, Yuan Li, Zhiling Yan, Chujie Gao, Ruoxi Chen, Zhengqing Yuan, Yue Huang, Hanchi Sun, Jianfeng Gao, et al. Sora: A review on background, technology, limitations, and opportunities of large vision models. *arXiv preprint arXiv:2402.17177*, 2024. 4
- [28] Zhuoyi Yang, Jiayan Teng, Wendi Zheng, Ming Ding, Shiyu Huang, Jiazheng Xu, Yuanming Yang, Wenyi Hong, Xiaohan Zhang, Guanyu Feng, et al. Cogvideox: Text-to-video diffusion models with an expert transformer. *arXiv preprint arXiv:2408.06072*, 2024. 4
- [29] William Peebles and Saining Xie. Scalable diffusion models with transformers. In *Proceedings of the IEEE/CVF international conference on computer vision*, pages 4195–4205, 2023. 4
- [30] Lvmin Zhang, Anyi Rao, and Maneesh Agrawala. Adding conditional control to text-to-image diffusion models. In *Proceedings of the IEEE/CVF international conference on computer vision*, pages 3836–3847, 2023. 4
- [31] Hu Ye, Jun Zhang, Sibio Liu, Xiao Han, and Wei Yang. Ip-adapt: Text compatible image prompt adapter for text-to-image diffusion models. *arXiv preprint arXiv:2308.06721*, 2023.
- [32] Nataniel Ruiz, Yuanzhen Li, Varun Jampani, Yael Pritch, Michael Rubinstein, and Kfir Aberman. Dreambooth: Fine tuning text-to-image diffusion models for subject-driven generation. In *Proceedings of the IEEE/CVF conference on computer vision and pattern recognition*, pages 22500–22510, 2023.
- [33] Rinon Gal, Yuval Alaluf, Yuval Atzmon, Or Patashnik, Amit H Bermano, Gal Chechik, and Daniel Cohen-Or. An image is worth one word: Personalizing text-to-

- image generation using textual inversion. *arXiv preprint arXiv:2208.01618*, 2022. 4
- [34] Maxime Oquab, Timothée Darcet, Théo Moutakanni, Huy Vo, Marc Szafraniec, Vasil Khalidov, Pierre Fernandez, Daniel Haziza, Francisco Massa, Alaaeldin El-Nouby, et al. Dinov2: Learning robust visual features without supervision. *arXiv preprint arXiv:2304.07193*, 2023. 4
- [35] Emanuele Aiello, Umberto Michieli, Diego Valsesia, Mete Ozay, and Enrico Magli. Dreamcache: Finetuning-free lightweight personalized image generation via feature caching. In *Proceedings of the Computer Vision and Pattern Recognition Conference*, pages 12480–12489, 2025. 4
- [36] Li Hu, Xin Gao, Peng Zhang, Ke Sun, Bang Zhang, and Liefeng Bo. Animate anyone: Consistent and controllable image-to-video synthesis for character animation, 2024. 4
- [37] Z Wang. Image quality assessment: Form error visibility to structural similarity. *IEEE Trans. Image Process.*, 13(4):604–606, 2004. 5
- [38] Richard Zhang, Phillip Isola, Alexei A Efros, Eli Shechtman, and Oliver Wang. The unreasonable effectiveness of deep features as a perceptual metric. In *Proceedings of the IEEE conference on computer vision and pattern recognition*, pages 586–595, 2018. 5
- [39] Abhijay Ghildyal, Nabajeet Barman, and Saman Zadtootaghaj. Foundation models boost low-level perceptual similarity metrics. In *ICASSP 2025-2025 IEEE International Conference on Acoustics, Speech and Signal Processing (ICASSP)*, pages 1–5. IEEE, 2025. 5
- [40] Jerry Tessendorf et al. Simulating ocean water. *Simulating nature: realistic and interactive techniques. SIGGRAPH*, 1(2):5, 2001. 10
- [41] Adrian Constantin and Joachim Escher. Wave breaking for nonlinear nonlocal shallow water equations. *Acta Mathematica*, 181:229–243, 1998. 11

# A unified Benchmark for Multi-Frame Image Restoration under Severe Refractive Warping

## Supplementary Material

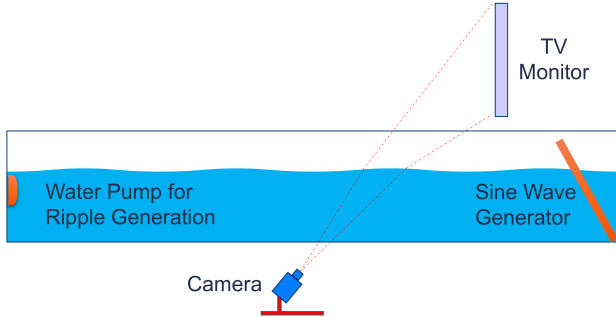


Figure 6. Data collection setup in the lab with water tank and water generators.

### 6. LAB setup

Figure 6. shows the laboratory data collection set up with a large water tank ( $20 \times 7 \times 3$  feet) which was filled with approximately 19-inch depth of water. A TV monitor was placed above the water to display a set of background images. The camera was set up below the water tank pointing towards the TV. During video recording, a wave generator at one end of the water tank produced disturbance on the water surface with a sine wave profile of a frequency between 1.0 to 2.8 Hz and wave amplitude ranging from 3 to 15mm peak-to-peak. Besides the sine wave generator, two water pumps were used to generate additional random ripple-like waves.

### 7. Wave generation

Table 5 provides parameters used to generate wave profiles. Details of specific wave types are provided below.

#### 7.1. Ocean Wave

For our simulation, we compute the Fast Fourier Transform (FFT) of Gerstner’s equations to represent the wave height as a random field over horizontal position and time. The height  $h(x, t)$  at the horizontal position  $\mathbf{x} = (x, z)$  can be expressed as

$$h(\mathbf{x}, t) = \sum_{\mathbf{k}} \tilde{h}(\mathbf{k}, t) \exp(i \mathbf{k} \cdot \mathbf{x}) \quad (1)$$

Where  $\tilde{h}(\mathbf{k}, t)$  denotes the complex spectral coefficient at wavevector  $\mathbf{k}$  and time  $t$ . This spectral form enables efficient analysis and synthesis of the surface, including fine

control over amplitudes and phases across the discretized wavenumber domain.

The wave height field is constructed using a spectral model that accounts for wind direction and speed. The Phillips spectrum [40] is used to define the wave amplitude at different wavenumbers. The spectrum is given by:

$$P_h(\mathbf{k}) = A \frac{\exp\left(-\frac{1}{(kL)^2}\right)}{k^4} |\hat{\mathbf{k}} \cdot \hat{\mathbf{w}}| \quad (2)$$

where  $P_h(\mathbf{k})$  is the power spectrum at wave vector  $\mathbf{k}$ ,  $A$  is an amplitude constant, and for a continuous wind of speed  $V$  the largest attainable scale is  $L = V^2/g$ , where  $g$  is gravitational acceleration and  $\hat{\mathbf{w}}$  denotes the unit vector in the wind direction.

Water-wave height fields can be modeled as Gaussian random fields whose spatial power follows a prescribed spectrum; the most efficient synthesis assigns the corresponding Fourier coefficients and then transforms to physical space.

$$\tilde{h}_0(\mathbf{k}) = \frac{1}{\sqrt{2}} (\xi_r + i \xi_i) \sqrt{P_h(\mathbf{k})} \quad (3)$$

The terms  $\xi_r$  and  $\xi_i$  are two independent random numbers drawn from a standard normal (Gaussian) distribution with mean 0, variance 1. After incorporating the Phillips spectrum, conjugate-symmetry, and dispersion, the Fourier amplitudes of the wave field realization [40] at time  $t$  in the frequency domain is:

$$\tilde{h}(\mathbf{k}, t) = \tilde{h}_0(\mathbf{k}) e^{i \omega(\mathbf{k})t} + \tilde{h}_0^*(-\mathbf{k}) e^{-i \omega(\mathbf{k})t} \quad (4)$$

Here,  $\tilde{h}_0$  is initial Fourier amplitude (at  $t = 0$ ). The height field in Eq. 4 preserves the complex conjugation property by propagating waves “to the left” and “to the right”. To obtain the spatial field  $h(\mathbf{x}, t)$ , we apply the inverse FFT to Eq. 4 and then compute the spatial gradients of the resulting height map to estimate surface normals and warping displacements. These normals and displacements are subsequently used to render wave-motion effects on the image.

#### 7.2. Sine Wave

The sine wave generation model simulates wave surfaces by representing the wave height field as a deterministic sinusoidal function propagating over a 2D spatial domain. This approach simplifies the complex, stochastic nature of waves

into a single-frequency wave, suitable for basic visualization or rendering applications. The wave can propagate horizontally with its motion animated over time to mimic wave dynamics. The wave height  $h$ , at position  $x$ ,  $z$  and time  $t$  (represented by discrete frames) is modeled as a plane wave using a sine function [18]. For image horizontal propagation, the wave height is:

$$h(x, t) = A \sin(k_x x - \omega t + \phi) \quad (5)$$

where  $A$  is the amplitude,  $\omega$  is the angular frequency, and  $x$  and  $y$  are spatial coordinates in a 2D domain, the  $\phi$  is the phase offset.

Sine wave is the extended version of the sine wave [19] to generalize to waves propagating in arbitrary directions by rotating  $h(x, t)$  with a random angle.

### 7.3. Shallow Water Wave

The shallow-water equations—derived as a depth-averaged form of the incompressible Navier–Stokes equations [41]—govern conservation of mass and horizontal momentum for a free-surface fluid [19]. Let  $h_{sh}$  be the surface height on a Eulerian mesh grid and  $(u, v)$  is the 2D velocity,  $\rho$  is the fluid density and  $g$  is the gravitational acceleration, then the differential equations can be written as

$$\frac{\partial(\rho h_{sh})}{\partial t} + \frac{\partial(\rho h_{sh} u)}{\partial x} + \frac{\partial(\rho h_{sh} v)}{\partial y} = 0 \quad (6)$$

$$\frac{\partial(\rho h_{sh} u)}{\partial t} + \frac{\partial(\rho h_{sh} u^2 + \frac{1}{2} \rho g h_{sh}^2)}{\partial x} + \frac{\partial(\rho h_{sh} uv)}{\partial y} = 0 \quad (7)$$

$$\frac{\partial(\rho h_{sh} v)}{\partial t} + \frac{\partial(\rho h_{sh} uv)}{\partial x} + \frac{\partial(\rho h_{sh} v^2 + \frac{1}{2} \rho g h_{sh}^2)}{\partial y} = 0 \quad (8)$$

## 8. Video generation

The distorted videos are generated by applying 200-frame-long series of precomputed wave normals to a selected background resized to  $512 \times 512$ . We mimic the LAB setup with camera located underwater and assume low field of view (parallel rays coming from the camera). The vector form of Snell’s law (Eq. 9) is applied to these rays,  $\vec{v}_1$ , at the water surface with  $\vec{N}$  surface normals to produce refracted rays  $\vec{v}_2$ .  $n_1$  and  $n_2$  are refractive indexes of water and air, respectively.

$$\vec{v}_2 = \frac{n_1}{n_2} \vec{N} \times (-\vec{N} \times \vec{v}_1) - \vec{N} \sqrt{1 - \left(\frac{n_1}{n_2}\right)^2 \|\vec{N} \times \vec{v}_1\|_2^2} \quad (9)$$

Finally, we compute the lateral displacement of the ray at a given distance to the background from the water surface

and generate 2D grid, which then is applied to the background producing the distorted frame. In our experiments we consider four levels of distortion to benchmark model responses in different regimes. We reuse the same wave profiles but scale the degree of deformation both by scaling the distance to the background and surface normals as  $\vec{N}' = (1 - \alpha) \cdot \vec{N}_0 + \alpha \vec{N}$ , where  $\vec{N}_0$  is the vertical normal representing a flat surface. This heuristic enables control of the degree of distortion, and we set the coefficients to ensure average std displacement of 0.002, 0.006, 0.018, and 0.054 relative to the image size for low, mid, high, and extreme wave amplitude in all sets regardless the wave type. Since evaluation of refracted rays for each pixel becomes computationally expensive at large image size and long sequence length, we implemented the above procedure on GPU using Pytorch library enabling fast sample generation both in training and inference.

## 9. Evaluation on the synthetic data

Table 5-Table 8 provide a full summary of the evaluation on ocean, shallow water, sine, and ripple waves at low, mid, high, and extreme levels of distortion. Pixel (PSNR and SSIM) and perception metrics (LPIPS, DINO, CLIP) are used. Entire video setup refers to evaluation of the metric for each frame in the video and then averaging. Comparison of this benchmark to the first frame setup may give a clue about variability over the video.

Table 5. Evaluation for ocean waves. L, M, H, E — low, medium, high, extreme wave amplitude. (\*) refers to evaluation on multiple output frames and average the metric.

Setup (ocean waves)	PSNR $\uparrow$	SSIM $\uparrow$	LPIPS <sub>VGG</sub> $\downarrow$	LPIPS <sub>Alex</sub> $\downarrow$	DINO $\downarrow$	CLIP $\downarrow$
<i>First frame</i>						
L	23.43	0.813	0.075	0.016	0.339	0.066
M	17.92	0.585	0.186	0.097	0.827	0.177
H	14.47	0.437	0.356	0.237	1.981	0.416
E	11.76	0.343	0.527	0.457	3.462	0.749
<i>Entire video*</i>						
L	21.78	0.754	0.096	0.055	0.432	0.086
M	16.71	0.524	0.227	0.125	1.077	0.227
H	13.39	0.389	0.425	0.310	2.515	0.530
E	10.88	0.305	0.586	0.544	3.980	0.888
<i>Pixel average</i>						
L	27.69	0.866	0.172	0.199	0.729	0.160
M	21.26	0.628	0.417	0.442	2.251	0.490
H	17.40	0.469	0.608	0.628	3.606	0.793
E	14.71	0.417	0.660	0.735	3.824	0.862
<i>Grid deformation</i>						
L	25.19	0.813	0.215	0.182	0.736	0.205
M	19.51	0.608	0.367	0.360	1.664	0.405
H	15.87	0.481	0.481	0.231	2.493	0.560
E	12.70	0.387	0.590	0.615	3.778	0.861
<i>Grid registration*</i>						
L	25.44	0.874	0.071	0.042	0.301	0.060
M	20.65	0.721	0.144	0.079	0.655	0.137
H	15.08	0.466	0.366	0.251	2.067	0.454
E	11.39	0.324	0.572	0.520	3.842	0.870
<i>DATUM*</i>						
L	26.19	0.863	0.125	0.078	0.396	0.089
M	21.09	0.718	0.229	0.147	0.902	0.198
H	15.60	0.468	0.457	0.353	2.533	0.533
E	12.05	0.312	0.621	0.584	4.023	0.842
<i>V-cache A5</i>						
L	23.95	0.789	0.134	0.077	0.045	0.407
M	23.46	0.772	0.138	0.077	0.397	0.120
H	21.16	0.672	0.186	0.100	0.640	0.171
E	16.54	0.502	0.331	0.207	1.594	0.372
<i>V-cache A3</i>						
L	24.86	0.813	0.126	0.075	0.373	0.114
M	24.27	0.798	0.120	0.073	0.289	0.092
H	22.22	0.717	0.157	0.089	0.449	0.129
E	18.11	0.559	0.157	0.268	1.102	0.263

Table 6. Evaluation for shallow water waves. L, M, H, E — low, medium, high, extreme wave amplitude. (\*) refers to evaluation on multiple output frames and average the metric.

<b>Setup (shallow water waves)</b>	<b>PSNR<math>\uparrow</math></b>	<b>SSIM<math>\uparrow</math></b>	<b>LPIPS<sub>VGG</sub><math>\downarrow</math></b>	<b>LPIPS<sub>Alex</sub><math>\downarrow</math></b>	<b>DINO<math>\downarrow</math></b>	<b>CLIP<math>\downarrow</math></b>
<i>First frame</i>						
L	21.71	0.733	0.099	0.059	0.489	0.101
M	16.65	0.492	0.264	0.149	1.370	0.296
H	13.27	0.374	0.503	0.399	3.160	0.692
E	10.84	0.292	0.610	0.580	4.244	0.899
<i>Entire video*</i>						
L	20.68	0.682	0.113	0.064	0.512	0.108
M	16.07	0.462	0.273	0.150	1.384	0.293
H	12.92	0.362	0.501	0.392	3.171	0.682
E	10.52	0.283	0.616	0.593	4.345	0.936
<i>Pixel average</i>						
L	25.67	0.800	0.204	0.228	0.821	0.197
M	20.03	0.536	0.446	0.427	2.468	0.509
H	16.52	0.432	0.612	0.606	3.606	0.793
E	14.08	0.404	0.671	0.750	3.921	0.875
<i>Grid deformation</i>						
L	20.76	0.648	0.328	0.326	1.370	0.354
M	17.29	0.496	0.413	0.386	1.991	0.466
H	14.21	0.413	0.551	0.525	3.401	0.735
E	11.64	0.352	0.636	0.668	4.377	0.937
<i>Grid registration*</i>						
L	24.81	0.846	0.076	0.045	0.318	0.068
M	19.51	0.646	0.180	0.096	0.855	0.183
H	13.94	0.397	0.464	0.336	2.791	0.628
E	10.88	0.297	0.607	0.575	4.246	0.925
<i>DATUM*</i>						
L	23.43	0.806	0.137	0.026	0.420	0.098
M	19.51	0.646	0.289	0.174	1.225	0.275
H	13.66	0.374	0.533	0.434	3.306	0.689
E	11.24	0.295	0.640	0.634	4.435	0.920
<i>V-cache A5</i>						
L	23.35	0.772	0.135	0.078	0.394	0.119
M	20.85	0.673	0.165	0.090	0.521	0.151
H	17.45	0.514	0.256	0.137	1.025	0.258
E	13.89	0.394	0.454	0.321	2.613	0.579
<i>V-cache A3</i>						
L	23.92	0.788	0.125	0.077	0.359	0.110
M	20.83	0.674	0.151	0.090	0.428	0.127
H	17.17	0.507	0.247	0.140	0.966	0.241
E	14.17	0.406	0.415	0.280	2.220	0.496

Table 7. Evaluation for sine waves. L, M, H, E — low, medium, high, extreme wave amplitude. (\*) refers to evaluation on multiple output frames and average the metric.

<b>Setup (sine waves)</b>	<b>PSNR<math>\uparrow</math></b>	<b>SSIM<math>\uparrow</math></b>	<b>LPIPS<sub>VGG</sub><math>\downarrow</math></b>	<b>LPIPS<sub>Alex</sub><math>\downarrow</math></b>	<b>DINO<math>\downarrow</math></b>	<b>CLIP<math>\downarrow</math></b>
<i>First frame</i>						
L	21.37	0.716	0.099	0.055	0.413	0.085
M	16.61	0.507	0.213	0.115	0.956	0.209
H	13.41	0.399	0.380	0.276	2.223	0.455
E	10.90	0.320	0.544	0.501	3.639	0.804
<i>Entire video*</i>						
L	21.38	0.716	0.099	0.055	0.417	0.086
M	16.64	0.506	0.214	0.312	0.962	0.209
H	13.42	0.397	0.381	0.278	2.238	0.452
E	10.81	0.315	0.547	0.507	3.683	0.808
<i>Pixel average</i>						
L	25.82	0.809	0.196	0.172	0.984	0.431
M	20.20	0.568	0.383	0.065	2.217	1.777
H	16.78	0.446	0.521	0.468	3.285	3.110
E	14.18	0.398	0.618	0.636	3.946	4.039
<i>Grid deformation</i>						
L	20.76	0.649	0.326	0.323	1.349	0.351
M	17.24	0.505	0.393	0.366	1.769	0.423
H	14.14	0.417	0.491	0.458	2.746	0.584
E	11.64	0.353	0.595	0.609	3.942	0.842
<i>Grid registration*</i>						
L	25.84	0.872	0.067	0.040	0.287	0.054
M	21.41	0.739	0.113	0.149	0.478	0.103
H	14.96	0.457	0.327	0.217	1.831	0.383
E	11.20	0.324	0.542	0.490	3.629	0.811
<i>DATUM*</i>						
L	26.02	0.855	0.121	0.077	0.380	0.084
M	19.68	0.644	0.245	0.087	0.937	0.209
H	14.94	0.441	0.454	0.338	2.515	0.521
E	11.65	0.319	0.613	0.575	3.994	0.840
<i>V-cache A5</i>						
L	22.95	0.747	0.152	0.091	0.501	0.190
M	22.68	0.734	0.150	0.312	0.467	0.137
H	20.54	0.640	0.190	0.105	0.680	0.176
E	15.70	0.489	0.343	0.237	1.834	0.399
<i>V-cache A3</i>						
L	23.87	0.769	0.153	0.093	0.545	0.153
M	23.12	0.756	0.141	0.086	0.430	0.126
H	22.07	0.715	0.150	0.091	0.448	0.128
E	16.70	0.532	0.288	0.198	1.340	0.304

Table 8. Evaluation for ripples waves. L, M, H, E — low, medium, high, extreme wave amplitude. (\*) refers to evaluation on multiple output frames and average the metric.

<b>Setup (ripples)</b>	<b>PSNR<math>\uparrow</math></b>	<b>SSIM<math>\uparrow</math></b>	<b>LPIPS<sub>VGG</sub><math>\downarrow</math></b>	<b>LPIPS<sub>Alex</sub><math>\downarrow</math></b>	<b>DINO<math>\downarrow</math></b>	<b>CLIP<math>\downarrow</math></b>
<i>First frame</i>						
L	20.66	0.712	0.129	0.077	0.678	0.138
M	16.12	0.502	0.327	0.218	1.865	0.418
H	13.07	0.384	0.521	0.430	3.434	0.746
E	10.49	0.259	0.622	0.604	4.500	0.913
<i>Entire video*</i>						
L	20.71	0.712	0.127	0.076	0.670	0.137
M	16.15	0.502	0.326	0.217	1.688	0.387
H	13.06	0.383	0.521	0.429	3.345	0.740
E	10.49	0.260	0.621	0.602	4.489	0.910
<i>Pixel average</i>						
L	25.01	0.806	0.214	0.185	1.203	0.222
M	19.69	0.564	0.400	0.326	2.459	0.481
H	16.41	0.443	0.556	0.485	3.665	0.730
E	13.86	0.360	0.642	0.678	4.481	0.885
<i>Grid deformation</i>						
L	21.59	0.682	0.337	0.339	1.485	0.376
M	18.24	0.555	0.433	0.420	2.379	0.541
H	14.37	0.428	0.564	0.561	3.711	0.795
E	11.36	0.321	0.641	0.683	4.678	0.936
<i>Grid registration*</i>						
L	25.93	0.888	0.063	0.039	0.263	0.056
M	16.89	0.533	0.313	0.196	1.688	0.387
H	13.12	0.380	0.517	0.413	3.345	0.740
E	11.02	0.310	0.571	0.523	3.953	0.857
<i>DATUM*</i>						
L	22.07	0.753	0.172	0.103	0.591	0.136
M	17.49	0.549	0.362	0.252	1.858	0.403
H	13.88	0.389	0.553	0.471	3.593	0.752
E	11.35	0.258	0.661	0.681	4.629	0.923
<i>V-cache A5</i>						
L	23.69	0.778	0.142	0.081	0.458	0.133
M	21.94	0.708	0.168	0.091	0.567	0.160
H	17.73	0.529	0.323	0.178	1.616	0.380
E	12.40	0.332	0.576	0.527	4.127	0.885
<i>V-cache A3</i>						
L	24.02	0.784	0.142	0.085	0.492	0.138
M	22.79	0.741	0.148	0.083	0.460	0.132
H	18.32	0.567	0.274	0.151	1.235	0.281
E	12.96	0.361	0.538	0.462	3.705	0.775